

Electromagnetic response of broken-symmetry nano-scale clusters

Ilya Grigorenko and Stephan Haas

Department of Physics and Astronomy, University of Southern California, Los Angeles, CA 90089-0484

A.F.J. Levi

Department of Physics and Astronomy, University of Southern California, Los Angeles, CA 90089-0484 and

Department of Electrical Engineering, University of Southern California, Los Angeles, CA 90089-2533

(Dated: September 16, 2018)

A microscopic, non-local response theory is developed to model the interaction of electromagnetic radiation with inhomogeneous nano-scale clusters. The breakdown of classical continuum-field Mie theory is demonstrated at a critical coarse-graining threshold, below which macroscopic plasmon resonances are replaced by molecular excitations with suppressed spectral intensity.

The prevalent classical model describing the interaction of visible and infrared electromagnetic radiation with nano-scale metallic clusters is based on Mie theory [1]. This local continuum field model which employs empirical values of a bulk material's linear optical response has been used to describe plasmon resonances in nanoparticles [2, 3, 4]. However, such a semi-empirical continuum description necessarily breaks down beyond a certain level of coarseness introduced by atomic length scales. Thus, it cannot be used to describe the interface between quantum and macroscopic regimes. Moreover, extensions of Mie theory to inhomogeneous cluster shapes are commonly restricted to low order harmonic expansions (e.g. elliptical distortions) and so do not exhaust the full realm of possible structures. In addition, near-field applications, such as surface enhanced Raman scattering [5], are most naturally described using a real-space theory that includes the *non-local* electronic response of inhomogeneous structures, again beyond the scope of Mie theory.

Ignoring the limitations of Mie theory can lead to conclusions of limited validity and usefulness. For example, it was recently argued [4] that resonances in the long wavelength limit are exclusively controlled by the object's shape, but otherwise *scale-invariant*, so that scaling of nanoparticles would not alter their characteristic plasmon frequencies. In particular, it was stated that an infinitely long elliptic rod, whose surface in Cartesian coordinates is defined by $(x/a)^2 + (y/b)^2 = R^2$, has two geometric *scalable* plasmon resonances that depend only on the ratio between semi-axis lengths a and b . In this work we develop a microscopic model that demonstrates the breakdown of this concept at atomic scales, whereas for large cluster sizes the classical predictions for the plasmon resonances are reproduced. We then show how this approach is useful in describing the coexistence of excitations of quantum and classical character in inhomogeneous structures on the nanoscale.

To capture the main single-particle and collective aspects of light-matter interaction in an inhomogeneous nanoscale system we adopt the well established linear response approximation [6]. Starting from the Schrödinger equation for noninteracting electrons with mass m_e and charge e moving in potential $V(\mathbf{r})$ we have

$$H\Psi_i(\mathbf{r}) = \left(-\frac{\hbar^2}{2m_e}\nabla^2 + V(\mathbf{r})\right)\Psi_i(\mathbf{r}) = E_i\Psi_i(\mathbf{r}). \quad (1)$$

Eq. 1 is solved simultaneously with the Poisson equation that determines the local potential due to the spatial distribution of the positive background charges. Using the jellium approximation, the resulting potential is implicitly given by $\nabla^2 V(\mathbf{r}) = 4e\pi\rho(\mathbf{r})$, where the density of the positive background charge $\rho(\mathbf{r})$ satisfies the condition of neutrality inside the nanostructure so that $\int \rho(\mathbf{r})d\mathbf{r} = N_{el}$, where N_{el} is the number of electrons.

Within linear response theory [7, 8], the induced electron charge density due to an external field of frequency ω is given by $\rho_{ind}(\mathbf{r}, \omega) = \int \chi(\mathbf{r}, \mathbf{r}', \omega)\phi_{tot}(\mathbf{r}', \omega)d\mathbf{r}'$, where the total self-consistent potential is determined by $\phi_{tot}(\mathbf{r}', \omega) = \phi_{ext}(\mathbf{r}', \omega) + \phi_{ind}(\mathbf{r}', \omega)$. Because the significance of non-local effects for inhomogeneous systems, including spatial dispersion of the dielectric function, is widely recognized [9, 10], for an inhomogeneous cluster of arbitrary shape we use the non-local density-density response function $\chi(\mathbf{r}, \mathbf{r}', \omega)$ that may be determined from a real-space representation [2]. Within the random phase approximation [8] one finds $\chi(\mathbf{r}, \mathbf{r}', \omega) = \sum_{i,j} \frac{f(E_i) - f(E_j)}{E_i - E_j - \hbar\omega - i\gamma} \Psi_i^*(\mathbf{r})\Psi_i(\mathbf{r}')\Psi_j^*(\mathbf{r}')\Psi_j(\mathbf{r})$,

where $f(E_i)$ is the Fermi filling factor and the small constant γ describes level broadening. Electron eigenenergies E_i and eigenfunctions Ψ_i are obtained numerically using a 6th order real-space discretization of the Schrödinger equation in three dimensions with a star-like stencil on a simple cubic lattice. Unless explicitly stated otherwise, zero Dirichlet boundary conditions are used to calculate the electron wave functions in this paper. The large scale sparse eigenproblem is solved using ARPACK [11]. The induced potential ϕ_{ind} is determined from the self-consistent integral

equation

$$\begin{aligned} \phi_{\text{ind}}(\mathbf{r}, \omega) = & \sum_{i,j} \frac{f(E_i) - f(E_j)}{E_i - E_j - \hbar\omega - i\gamma} \int \frac{\Psi_i^*(\mathbf{r}') \Psi_j(\mathbf{r}')}{|\mathbf{r} - \mathbf{r}'|} d\mathbf{r}' \\ & \times \int \Psi_j^*(\mathbf{r}'') \phi_{\text{tot}}(\mathbf{r}', \omega) \Psi_i(\mathbf{r}'') d\mathbf{r}'', \end{aligned} \quad (2)$$

and the induced field is found via $\mathbf{E}_{\text{ind}}(\mathbf{r}, \omega) = -\nabla \phi_{\text{ind}}(\mathbf{r}, \omega)$. For sufficiently small structures, when the typical wavelength of the external radiation is larger than the structure, retardation effects can be ignored. Note, that the induced field is not necessarily collinear with the applied external field $\mathbf{E}_{\text{ext}}(\mathbf{r})$.

The integral equation Eq.(2) is discretized on a real-space mesh, using a simple cubic lattice with lattice constant L . The natural energy scale E_0 is defined by $E_0 = \hbar^2/(2m_e L^2)$. For example, in the case of GaAs 1D nanorods [12] with conduction band carrier density 10^{18} cm^{-3} the discretization lattice length scale is $L = 1.28 \text{ nm}$, the density $\rho = 1/480$ in units of L^{-3} and the energy scale $E_0 = 330 \text{ meV}$.

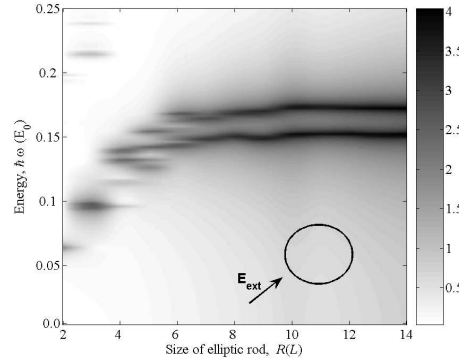


FIG. 1: Logarithm of the energy of the induced electric field ($\log_{10}(W_{\text{ind}})$) (see text) in an elliptic metallic rod due to applied external field \mathbf{E}_{ext} along the $(1, 1, 0)$ direction as a function of face surface size R and photon energy $\hbar\omega$ of the external field in units of E_0 . Aspect ratio (semi-minor to semi-major axis) $a : b = 1 : 1.3$. Cross section of the elliptical rod and the vector of the applied external field \mathbf{E}_{ext} are depicted in the lower right corner. Temperature $T = 0 \text{ K}$, carrier density $\rho = (1/480) L^{-3}$, and $\gamma = 10^{-3} E_0$. All real space calculations are performed on a mesh of simple cubic geometry with lattice constant L .

We illustrate the application of this approach to an infinitely long elliptic rod illuminated by an external field. The rod is aligned in the z direction and the electric field polarization is along the $(1, 1, 0)$ direction. For the wave functions we assume periodic boundary conditions along the z direction. To quantify the response of arbitrary geometries to the applied field, we calculate the energy of the induced field, defined by $W_{\text{ind}}(\omega) = (1/2) \int |\mathbf{E}_{\text{ind}}(\mathbf{r}, \omega)|^2 d\mathbf{r}$. In Fig. 1 logarithm of the energy of the induced field ($\log_{10}(W_{\text{ind}})$) is displayed as a function of the applied external field photon energy $\hbar\omega$ and the characteristic system size R for the aspect ratio $a : b = 1 : 1.3$. For sufficiently large rod sizes, one clearly observes two plasmon resonances, ω_+ and ω_- , consistent with earlier predictions based on Mie theory [4]. Our method confirms that these resonances occur at $\omega_+ = \omega_p(b/(a+b))^{1/2}$ and $\omega_- = \omega_p(a/(a+b))^{1/2}$, where ω_p is the bulk plasmon frequency $\omega_p = \sqrt{4\pi e^2 \rho / m_e}$. The grey scale in Fig. 1 is on a logarithmic scale, demonstrating that the spectral intensity for large rod sizes is orders of magnitude greater compared to smaller rod sizes. Most importantly, it is evident from this figure that the classical picture of two well-defined resonances breaks down below a characteristic system size. For sufficiently small rod sizes, the two macroscopic resonances split into multi-level molecular excitations, with the overall spectral weight shifting towards lower energies. For the chosen parameters this transition occurs at $R_c \approx 6.5 L$. Below R_c , the spectral intensity of the energy levels is reduced because fewer electrons participate in the individual resonances. The physics determining the value of R_c may be illustrated considering an infinitely long cylindrical rod of radius R and electron density ρ . In the classical regime, the observed collective oscillations are only weakly damped, indicating that they are well separated from the quasi-continuum of single-particle excitations. This leads to the condition $\omega_p R / v_F \gg 1$, stating that the plasmon phase velocity is greater than the Fermi velocity v_F of the electrons [13]. For $r < R$ the electrons are trapped in a harmonic potential due to the uniform positive background [14] and the characteristic collective frequency is $\omega_p = \sqrt{4\pi e^2 \rho / (2m_e)}$. Estimating the Fermi velocity using a bulk value $v_F = (3\pi^2 \rho)^{1/3} \hbar / m_e$ one obtains $R \gg R_c = \frac{\pi^{1/6} 3^{1/3}}{\sqrt{2}} \frac{\hbar}{e m_e^{1/2} \rho^{1/6}} \approx 3.4 L$ for an electron density $\rho = (1/480) L^{-3}$, which is in reasonable, but only approximate, agreement with the calculated threshold $R_c \approx 6.5 L$ shown in Fig. 1.

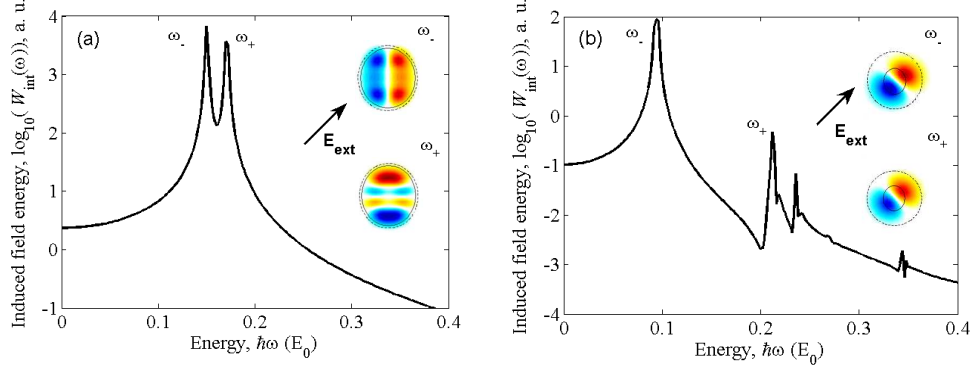


FIG. 2: (a) Logarithm of the energy of the induced electric field ($\log_{10}(W_{\text{ind}})$) in an elliptic rod of size $R = 11 L$ with aspect ratio $a : b = 1 : 1.3$ as a function of photon energy $\hbar\omega$ of the external field in units of E_0 . Carrier density $\rho = (1/480) L^{-3}$ and $\gamma = 10^{-3} E_0$. The direction of the external field is indicated by the arrow. Inset: induced charge density at the resonant frequencies ω_+ and ω_- . The boundary of the rod is shown using the solid line, and the dotted line shows the set of classical turning points, corresponding to the positive background potential. (b) Same as (a), but for size $R = 3 L$.

For system sizes below R_c the dominant excitations are observed to shift towards lower energies as the positive background potential becomes increasingly anharmonic. The harmonicity criterion for excitations can be expressed as $\sigma_0/R \leq 1$, where $\sigma_0 = (\frac{\hbar}{m_e \omega_p})^{1/2}$ is the classical turning point for an electron in the ground state of the harmonic potential. This is equivalent to the condition $R \geq R_c = (\frac{\hbar^2}{2m_e \rho e^2})^{1/4}$, yielding $R \geq 3 L$.

The nature of the excitations changes as the characteristic size R crosses the quantum threshold R_c . In Fig. 2, we show logarithm of the calculated energy of the induced field ($\log_{10}(W_{\text{ind}})$) as a function of external field frequency. As shown in Fig. 2(a), for relatively large rod sizes, the two distinct plasmon resonances labelled ω_- and ω_+ correspond to two orthogonal bipolar charge distributions, as indicated in the inset. The spatial orientations of these induced resonances are aligned with the semi-major and semi-minor axes, and do not depend on the direction of the incident field. In contrast, for system sizes less than R_c (Fig. 2(b)), the excitation spectrum consists of several lower-intensity modes, dominated by a low frequency resonance. However, the spatial characteristics of these modes are different from the classical limit, i.e. they are *aligned* with the incident field, indicating that Mie theory breaks down in the quantum regime.

An advantage of the self-consistent non-local response theory described in this work is that it extends naturally to inhomogeneous structures with nano-scale and atomically sharp edges and corners. This is of great practical interest to nano-photonic applications since such features are commonly associated with substantial local field enhancements [5]. However, the intuition driving such expectations is usually derived from classical continuum field theory which may not be applicable in this regime. When investigating structures at the microscopic level one needs to account quantitatively for changes in the response spectrum. One would also like to describe the breakdown of the continuum picture and quantum-mechanical discretization effects which may ultimately lead to new and interesting functionalities that are accessible by nano-scale engineering.

To explore this we consider a representative asymmetric nanostructured system of material volume $V_{\text{mat}} = 5516 L^3$ consisting of a conjoined sphere and rectangular bar (Fig. 3(a)) whose response strongly depends on the carrier concentration (Fig. 3(b)). Plots of induced charge distributions in response to an external electric field are shown for different carrier concentrations and frequencies of the incident radiation.

For $N_{\text{el}} = 100$ in the low-frequency limit (Fig. 3(c)), this leads to a dipole-like anisotropic response for which the induced field is not collinear to the external field \mathbf{E}_{ext} (indicated by the arrow). Note, that in this case the induced charge is localized within the boundaries of the nanostructure, and follows the nanostructure's physical bounds given by the positive charge distribution, in agreement with expectations from classical field theory. At this relatively high carrier concentration and at a high external field frequency of $\omega = 0.415 E_0$, one observes a complex local enhancement of the induced charge density (Fig. 3(d)). For the low carrier concentration ($N_{\text{el}} = 5$), shown in Fig. 3(e) and (f) the induced charge density arises from excitation of low energy eigenstates and the overall response is weaker. Note, the induced charge is not localized within the boundaries of the nanostructure. Varying the carrier concentration hence acts as a “switch” that can activate different resonant regions in a broken-symmetry atomic-scale structure.

At higher frequencies, the system response can be even more complex. For example, in the case of low carrier concentrations and resonance frequency $\omega = 0.085 E_0$, the induced dipole field is rotated with respect to the static

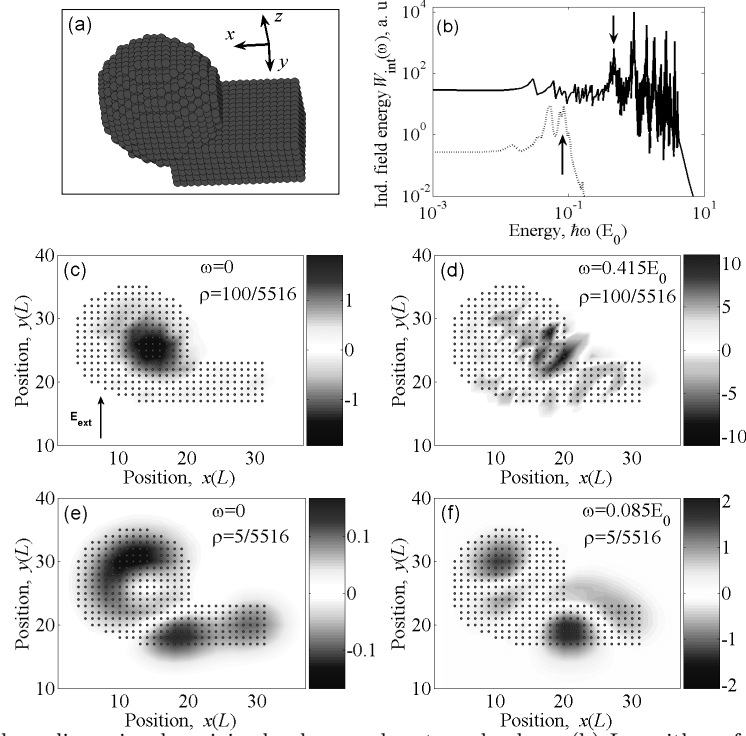


FIG. 3: (a) Illustration of three-dimensional conjoined sphere and rectangular bar. (b) Logarithm of the induced field energy in the structure for $N_{\text{el}} = 100$ (solid line) and $N_{\text{el}} = 5$ (dotted line) as a function of the external field frequency. The material volume is $V_{\text{mat}} = 5516 L^3$. The arrows in the figure show the frequencies chosen for results of calculations shown in (d) and (f). Induced charge density for a nanoscale asymmetric structure for the indicated charge densities and frequencies of the external field. Temperature $T = 0$ K and $\gamma = 10^{-3} E_0$. (c) $N_{\text{el}} = 100$, $\hbar\omega = 0$, the direction of the external field is indicated by the arrow; (d) $N_{\text{el}} = 100$, $\hbar\omega = 0.415 E_0$. (e) $N_{\text{el}} = 5$, $\hbar\omega = 0$. (f) $N_{\text{el}} = 5$, $\hbar\omega = 0.085 E_0$.

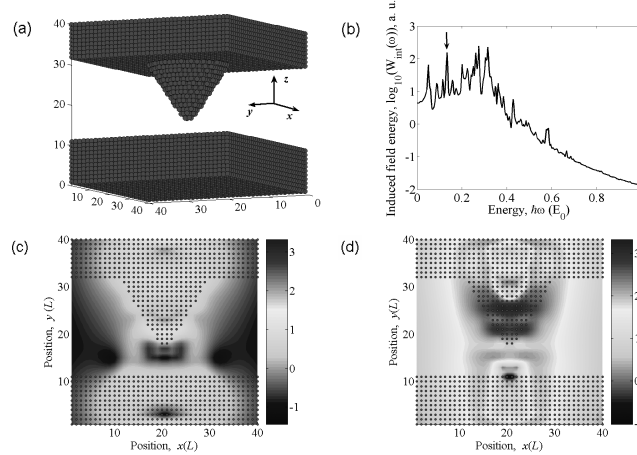


FIG. 4: (a) Three-dimensional image of a structure consisting of a sharp tip and two parallel flat plates of material volume $V_{\text{mat}} = 33404 L^3$ containing $N_{\text{el}} = 207$ electrons. The incident electric field is along the $(0, 0, 1)$ direction, temperature $T = 0$ K and $\gamma = 10^{-3} E_0$. (b) Logarithm of the induced electric field energy in the structure as a function of the field frequency, the arrow shows the frequency chosen for results of calculations shown in (d). (c) Logarithm of the intensity of the induced electric field ($\log_{10}(|\mathbf{E}_{\text{ind}}(\mathbf{r})|^2)$) in static limit, $\hbar\omega = 0$. (d) At resonance, $\hbar\omega = 0.135 E_0$.

limit (Fig. 3(f)). Hence, by tuning the frequency of the external field, discrete quantum states within anisotropic nanostructures can either be accessed or avoided. This control exposes various quantum functionalities that are beyond conventional Mie theory.

As an example, let us consider the induced electric field at the interface between a sharp tip and a flat surface illuminated by plane-wave radiation incident in the z direction (Fig. 4(a)). The total material volume of the system is $V_{\text{mat}} = 33404 L^3$.

In the static limit, a moderate enhancement of field intensity is found in close proximity to the tip. Results of calculating logarithm of the induced field intensity ($\log_{10}(|\mathbf{E}_{\text{ind}}(\mathbf{r})|^2)$) are shown in Fig. 4(c). While most of the induced charge density accumulates at the surface, there is considerable penetration into the bulk. In contrast, when the same structure is illuminated at resonance, the induced plasmonic response is much more intense than the low frequency limit. Here, the induced field intensity increases by 2 orders of magnitude, while the spatial dispersion of the “hot spot”, as measured by full width half maximum, remains approximately the same (see Fig. 4(d)). This demonstrates that custom-designed atomic-scale tip structures may be used to control the near field and fully quantum-mechanical modeling can quantitatively account for local enhancements, as well as screening and focusing effects.

In summary, a non-local response theory describing the interaction of electromagnetic radiation with inhomogeneous nano-scale structures has been developed and implemented. This approach may be used to describe metals and semiconductors in the metallic regime. For simple geometries semi-empirical continuum-field Mie theory is found to break down beyond a critical coarseness. At this level of coarse graining, the response is no longer exclusively determined by particle shape. In more complex inhomogeneous geometries excitations of quantum and classical character can coexist. For objects with nano-scale sharp features, our real-space response theory uncovers new functionalities, such as local resonances that are activated by tuning the carrier concentration or the frequency of the incident field.

We acknowledge discussions with P. B. Littlewood and V. Kresin. This work is supported by DARPA. Computational facilities have been generously provided by the HPC Center at USC.

-
- [1] G. Mie, *Annalen der Physik*, **25**, 377 (1908).
 - [2] D. M. Wood and N. W. Ashcroft, *Phys. Rev. B* **25**, 6255 (1982); M. J. Rice, W. R. Schneider, and S. Strassler, *Phys. Rev. B* **8**, 474 (1973).
 - [3] Q. P. Li and S. DasSarma, *Phys. Rev. B* **43**, 11768 (1991).
 - [4] D. R. Fredkin and I. D. Mayergoyz, *Phys. Rev. Lett.* **91**, 253902 (2003).
 - [5] S. Nie and S. R. Emory, *Science* **275**, 1102 (1997).
 - [6] S. Pokrant and K. B. Whaley, *Eur. Phys. J. D* **6**, 255 (1998); P. Chen and K. B. Whaley, *Phys. Rev. B* **70**, 045311 (2004); J. Schrier and K. B. Whaley, *Phys. Rev. B* **72**, 085320 (2005); S. Lee, P. von Allmen, F. Oyafulso, G. Klimeck, and K. B. Whaley, *J. Appl. Phys.* **97**, 043706 (2005).
 - [7] J. Lindhard, *Kgl. Danske Videnskab. Selskab, Mat.-Fys. Medd.* **28** n. 8 (1954).
 - [8] H. Ehrenreich and M. H. Cohen, *Phys. Rev.* **115**, 786 (1959).
 - [9] F. J. Garcia de Abajo and P. M. Echenique, *Phys. Rev. B* **46**, 2663 (1992).
 - [10] K. Kempa, A. Liebsch, W. L. Schaich, *Phys. Rev. B* **38**, 12645 (1988).
 - [11] D.C. Sorensen, invited paper in *SVD and Signal Processing, III*, M. Moonen and B. De Moor (eds.), Elsevier Science, Amsterdam, (1995).
 - [12] H. G. Lee, H. C. Jeon, T. W. Kang, T. W. Kim, *Appl. Phys. Lett.* **78**, 3319 (2001).
 - [13] D. Pines, P. Nozieres, *The Theory of Quantum Liquids*, Vol. I, W. A. Benjamin, Inc., p. 55 (1966).
 - [14] V. V. Kresin, *Phys. Rep.* **220**, 1 (1992).